A robust and versatile platform for image scanning microscopy enabling super-resolution FLIM

Marco Castello[1,6], Giorgio Tortarolo [1,2,6], Mauro Buttafava[3], Takahiro Deguchi[4], Federica Villa[3], Sami Koho[1], Luca Pesce[4], Michele Oneto[4], Simone Pelicci[4], Luca Lanzanó [4], Paolo Bianchini[4], Colin J. R. Sheppard[4], Alberto Diaspro [4,5], Alberto Tosi [3] and Giuseppe Vicidomini [1]*

Image scanning microscopy (ISM) can improve the effective spatial resolution of confocal microscopy to its theoretical limit. However, current implementations are not robust or versatile, and are incompatible with fluorescence lifetime imaging (FLIM). We describe an implementation of ISM based on a single-photon detector array that enables super-resolution FLIM and improves multicolor, live-cell and in-depth imaging, thereby paving the way for a massive transition from confocal microscopy to ISM.

Fluorescence confocal laser-scanning microscopy (CLSM) is an indispensable tool for biomedical research[1] by virtue of its versatility, its optical-sectioning capability and its compatibility with spectroscopic assays such as fluorescence lifetime[2]. Spatial resolution is another important asset of CLSM, as closing the optical pinhole makes it possible to reduce the size of the CLSM point-spread function (PSF) by up to a factor of $\sim\sqrt{2}$ (full-width at half-maximum (FWHM)) with respect to conventional diffraction-limited microscopy. However, the reduction of the PSF does not always lead to a resolution enhancement, because closing the pinhole also causes a heavy signal loss, and thus a decrease of the signal-to-noise ratio (SNR). ISM overcomes this limitation and effectively attains the $\sqrt{2}$-fold resolution improvement predicted for CLSM.

Per the original concept[3], one can achieve ISM with a regular confocal laser-scanning microscope by replacing the classical single-point detector with a detector array and opening the pinhole (typically to 1 Airy unit (AU)) to collect most of the fluorescence light. The elements of the detector array generate a series of 'confocal' scanned images that differ in information content and are shifted with respect to one another. To form an ISM image, one can use the so-called pixel-reassignment (PR) method[3,4], in which all the scanned images are added together after each image is shifted by a vector (shift vector) that in the ideal case depicts the relative position of the corresponding detector element, properly scaled by a PR factor. In alternative methods, the scanned images are fused together by more advanced methods[5,6]. The final ISM image has a PSF equivalent to—or even smaller than—that of the 'ideal' (infinitely small pinhole) CLSM image, but it maintains a higher SNR, and thus a higher effective resolution.

In the first implementation of ISM, a conventional camera was used as the detector array[5], but the low camera frame rate severely limited the imaging speed. The speed limitation was addressed first by multi-spot-excitation ISM architectures[7,8] and later by several all-optical ISM implementations[9–13]. In all-optical ISM, the final image is obtained during the raster scan through superimposition of all the scanned images after upscaling of their position by the PR factor on a conventional camera. These setups do not need image reconstruction, but they do not give access to the raw scanned images and, because the upscaling is achieved through the use of a second synchronized scanner[9,12] or by passing the emission beam twice across the same scanner[11], they substantially modify the architecture of regular CLSM. A simplified all-optical ISM architecture was proposed recently[13]; however, it cannot implement a pinhole, and thus optical sectioning can be obtained only with the use of nonlinear contrast mechanisms, such as two-photon excitation. Furthermore, in all-optical ISM implementations, the PR factor needs to be decided before imaging. However, this task is complex because the PR factor strongly depends on the shape of the excitation and emission PSFs, which continuously changes as a result of the system, sample-induced distortions and imaging conditions—for example, the PR factor depends on the fluorophore Stokes shift[14]. Finally, because all-optical ISM implementations use conventional cameras, their combination with time-resolved spectroscopy, as in FLIM, is not straightforward.

More recently, the speed limit was solved in the AiryScan implementation of CLSM[15], in which a hexagonal bundle of optical fibers is connected to a one- dimensional array of GaAsP (gallium arsenide phosphide) photomultiplier tubes to mimic a detector array. However, this device does not synergistically integrate the temporal and spatial characteristics of single-point detectors and cameras, which would be fundamental for versatile ISM implementations. Single-photon avalanche diode (SPAD) arrays[16], however, offer everything required to fill this gap.

Here we demonstrate an ISM implementation based on a novel SPAD array module with 5×5 elements that is specifically designed for ISM (Supplementary Fig. 1, Supplementary Note 1). Insertion of this SPAD array module in the microscope detection arm (Fig. 1a) can transform any existing confocal laser-scanning microscope into an image scanning microscope, while preserving all CLSM functionality. Unlike with existing all-optical ISM implementations, the availability of the raw scanned images allowed us to implement an adaptive PR (APR) method in which the PR factor and, more generally, the shift vectors are obtained directly from the data, without the need for calibrations or prior information (Supplementary Note 2)[6]. Furthermore, the single-photon timing ability of the SPAD array made it possible to combine ISM with FLIM[17], thus enabling straightforward super-resolution FLIM.

[1]Molecular Microscopy and Spectroscopy, Istituto Italiano di Tecnologia, Genoa, Italy. [2]Dipartimento di Informatiche, Bioingegneria, Robotica e Ingegneria dei Sistemi, University of Genoa, Genoa, Italy. [3]Dipartimento di Elettronica, Informazione e Bioingegneria, Politecnico di Milano, Milan, Italy. [4]Nanoscopy and NIC@IIT, Istituto Italiano di Tecnologia, Genoa, Italy. [5]Dipartimento di Fisica, University of Genoa, Genoa, Italy. [6]These authors contributed equally: Marco Castello, Giorgio Tortarolo. *e-mail: giuseppe.vicidomini@iit.it

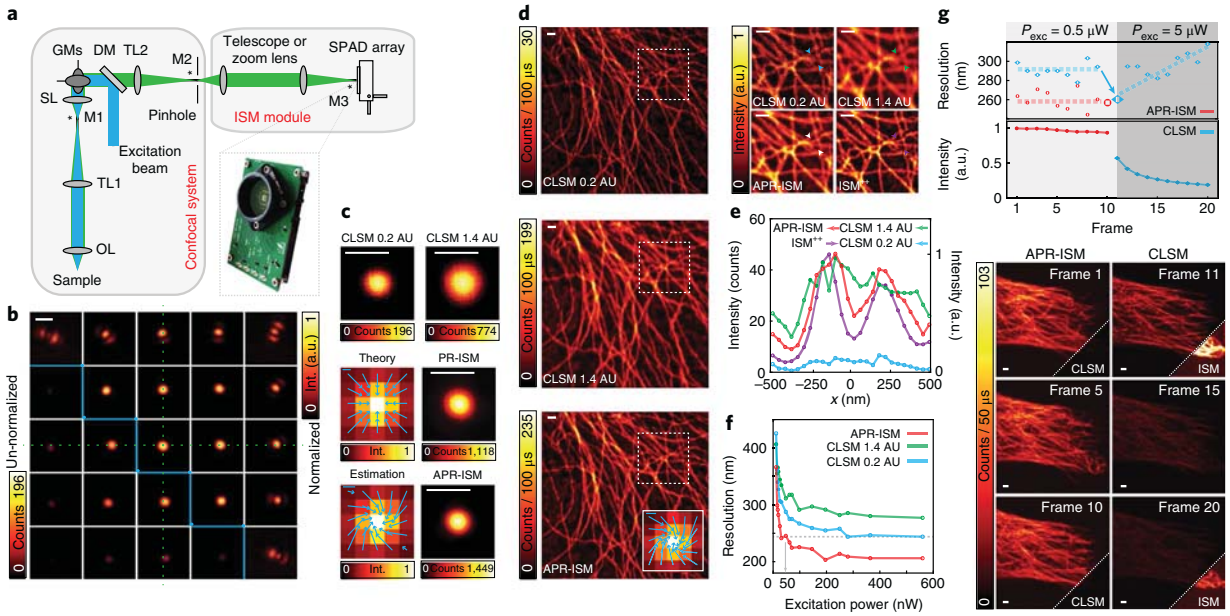

Fig. 1 | Image scanning microscopy with SPAD array. a, Schematic of the image scanning microscope. Excitation light (blue) passes the dichroic mirror (DM) and is deflected by the galvanometer mirrors (GMs). The pivot point of the scanner is projected by the scan lens (SL) and a tube lens (TL1) into the back aperture of the objective lens (OL). Fluorescence (green) is collected by the OL, descanned by the GMs, filtered by the DM and projected by a second tube lens (TL2) into the pinhole plane. A telescope or zoom lens is used to image the pinhole plane into the SPAD array and adds extra magnification (from M2 to M3) to match the physical size of the detector to 1.4 AU. Asterisks denote the planes conjugated. The image in the lower right shows the printed circuit board hosting the detector. **b**, Matrix representing the scanned reflection images of a single isolated gold bead (80 nm). Scanned images in the top right and bottom left corners are normalized to the maximum intensity of that image and to the maximum intensity of the central scanned image, respectively. Horizontal and vertical dashed green lines are present to guide the eye. Scale bar, 500 nm. **c**, Side-by-side comparison of the PSFs of the ideal confocal (0.2-AU pinhole), the open confocal (1.4-AU pinhole), PR-ISM (i.e., PR with the theoretical shift vectors) and APR-ISM (i.e., pixel reassignment with the estimated shift vectors). Scale bars, 500 nm. Fingerprint maps, superimposed with the theoretical and estimated shift vectors projected in the image plane, are also shown. Scale bars, 100 nm. **d**, Side-by-side comparison of ideal confocal, open confocal and APR-ISM images of tubulin filaments stained with Abberior STAR red. The inset in the APR-ISM image shows the fingerprint map and the estimated shift vectors. Scale bars, 100 nm. Also shown is a composite image including magnified views of the areas outlined by dashed boxes in the main images, together with the ISM image obtained by multi-image deconvolution (ISM^{++}; five iterations). Arrowheads indicate positions used to generate the data in **e**. Scale bars, 1 µm. Data are representative of $n = 10$ experiments. **e**, Line intensity profiles across two branching tubular filaments at the positions of the arrowheads in **d** for the different imaging modalities. **f**, FRC-based resolution as function of the excitation intensity for the different imaging modalities. **g**, Results of time-lapse (4 min, 20 frames) imaging of SiR-tubulin in live human HeLa cells ($n = 4$ experiments). Top, resolution and total fluorescence intensity (normalized at the first frame) as a function of the frame for CLSM (1.4 AU) and APR-ISM. The first 10 frames were collected with 0.5-µW excitation beam power, and at the 11th frame the excitation beam power was increased to 5 µW to achieve similar resolution between CLSM and ISM (large colored dots in the resolution plot). Bottom, representative frames of the time-lapse imaging. Scale bars, 1 µm. AU, Airy units; a.u., arbitrary units; int., intensity.

We first integrated our SPAD array module into a custom confocal laser-scanning microscope (Supplementary Fig. 2); its pinhole was completely open and its single-point detector was substituted by a telescope and the SPAD array module. The telescope conjugated the pinhole with the SPAD array and provided magnification such that the projected size of the full SPAD array was ~1 AU. Practically, the detector mimicked a 1-AU pinhole, which maintained the optical sectioning; notably, the need for a pinhole vanishes when advanced reconstruction methods, such as deconvolution, are used. As an initial demonstration of ISM with the SPAD array, we imaged a single isolated subdiffraction gold bead in reflection mode, thus measuring the system PSF. As shown in Fig. 1c, the PSF of the 'ideal' confocal (0.2 AU, central detector element) was reduced in size with respect to that of the 'open' confocal (1.4 AU, sum of all the detector elements) counterpart, from 281 nm to 213 nm (FWHM), but at the same time the peak signal intensity was substantially reduced. In contrast, the PSF of the ISM system (theoretical shift vectors) was similar to that of the ideal confocal (217 nm, FWHM), and the signal level was substantially improved, by ~5.7-fold compared with that of the ideal confocal and ~1.4-fold compared with that of the open confocal (Supplementary Fig. 3), yielding a super-brightness effect[4]. As the real shift vectors differed substantially from the theoretical ones (Fig. 1c), use of our new APR-ISM approach compensated for distortions and further improved the PSF to 193 nm; the peak signal intensity also improved (by ~1.8-fold and ~7.4-fold compared with that of the open and ideal confocal, respectively).

In fluorescence imaging, our method automatically adapted to the fluorophore Stokes shift and generated higher-quality images with respect to both ideal and open CLSM (Fig. 1d, Supplementary Figs. 4–6, Supplementary Table 1). We obtained a further enhancement in image quality by fusing the scanned images with an adaptive multi-image deconvolution algorithm (ISM^{++})[18] (Supplementary Note 3, Fig. 1d). We quantified the resolution enhancement provided by our APR-ISM method by plotting line intensity profiles across tiny and closely packed tubulin filaments (Fig. 1e) and via the Fourier ring correlation (FRC) method[19]. The FRC-based resolution as a function of the excitation beam power (Fig. 1f, Supplementary Fig. 7) showed the ability of APR-ISM to achieve the same resolution as ideal CLSM at one-tenth the illumination intensity. This reduction of illumination intensity represents a great benefit for live-cell imaging (Supplementary Figs. 8 and 9, Supplementary Videos 1–7). For example, ISM allowed super-resolution (~260 nm) time-lapse

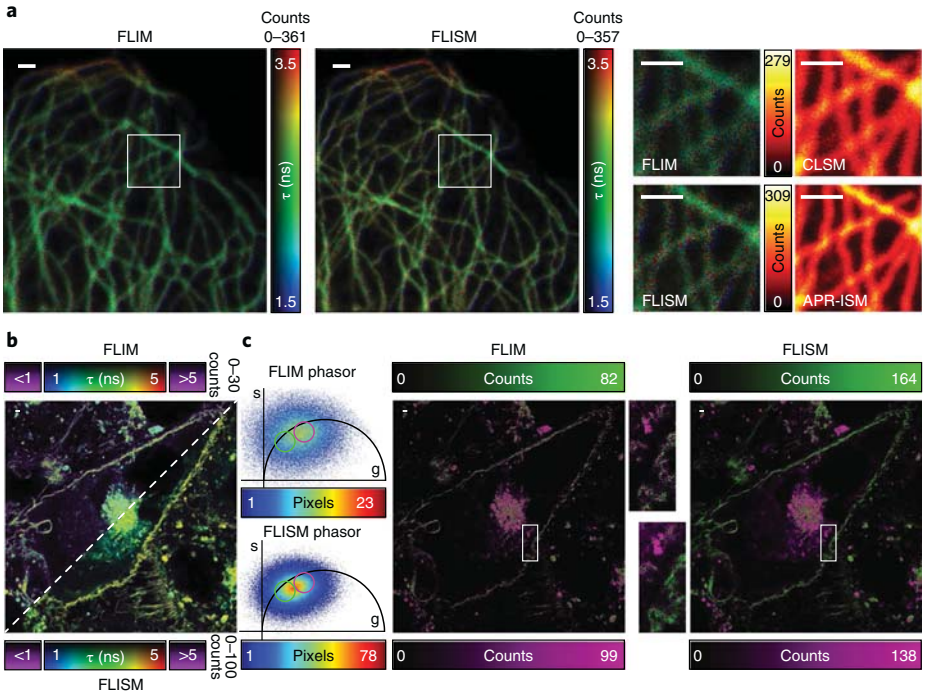

Fig. 2 | Fluorescence lifetime image scanning microscopy. a, Side-by-side comparison of fitting-based FLIM (left; 1.4 AU) and FLISM (center) images of tubulin labeled with Abberior STAR red, and magnified views of the regions outlined by white boxes in the main images, paired with the respective intensity images (right). Scale bars, 1 μm. Data are representative of $n = 4$ experiments. **b**, Comparison of fitting-based FLIM (top-left; 0.25 AU) and FLISM (bottom-right) images of membrane labeled with ANEP dye. Purple pixels correspond to out-of-range fluorescence lifetime values, which probably resulted from artifacts during the exponential fitting analysis. All pixels were analyzed. **c**, Left, comparison of the phasor plots for the FLIM and FLISM datasets (only the points/pixels above the background level are represented, i.e., 5 and 15 photons, respectively, for the FLIM and FLISM images). Right, the images obtained by back-projection of the points within the purple (long lifetime) and red (short lifetime) circles in the plots on the left, and magnified (3.1 ×) views of the regions outlined by white boxes ($n = 10$ experiments). Scale bars, 1 μm.

imaging of SiR-tubulin in live cells with negligible photobleaching (< 5% after ten frames). Conventional CLSM could achieve similar resolution only with increased illumination power (from 0.5 μW to 5 μW), and this led to greater photobleaching (> 75% after ten frames) and phototoxicity (Fig. 1g, Supplementary Videos 8–11).

To demonstrate that the proposed ISM implementation is compatible with time-resolved spectroscopy, in particular with fluorescence lifetime, we registered the photons in a time-tag modality by using a multi-channel time-to-digital converter. In fluorescence lifetime ISM (FLISM) (Fig. 2), the time-tagged data and the APR method are used to produce a three-dimensional (3D-FLISM) dataset (x,y,t), where the third dimension t (lag time) represents the photon-arrival-time histogram (Supplementary Fig. 10). Successively, we processed the 3D-FLISM dataset (similarly to the confocal 3D-FLIM dataset) via conventional fluorescence lifetime analysis methods, and found that with exponential fitting analysis it was possible to obtain a fluorescence lifetime image with higher resolution and precision than in the confocal FLIM counterpart (Fig. 2a,b, Supplementary Figs. 11 and 12). Although the overall photon timing jitter was the same for FLIM and FLISM (i.e., same laser, same detector, same optics, and same multi-channel time-to-digital converter), the precision of FLISM was higher owing to the higher SNR. The FLISM dataset also could be analyzed via the phasor approach (Fig. 2c). As an example, we imaged live cells with an ANEP polarity-sensitive membrane probe whose changes in fluorescence lifetime allowed us to distinguish domains of the membrane in liquid-ordered and liquid-disordered phases[20]. Again, thanks to the higher SNR, the points in the FLISM phasor plot were located more precisely than those in the FLIM counterpart, which allowed for better separation of domains in liquid-ordered and liquid-disordered phases.

Next, to demonstrate that our SPAD array module can pave the way for a transition from CLSM to ISM, we integrated it into a commercial confocal laser-scanning microscope (Supplementary Fig. 13). We added a zoom lens system to conjugate the SPAD array with the confocal pinhole and to allow fast changing of the magnification on the detector, which is needed when switching between different objective lenses. As an example, we used 20 × water (Fig. 3a) and 10 × glycerol (Fig. 3b) objective lenses to image (down to 0.9 mm and 1.8 mm for 20 × and 10 ×, respectively) E-YFP-expressing neurons in the cleared whole brain of a mouse. APR-ISM once again provided terrific SNR enhancement, giving effective access to the desired $\sqrt{2}$-fold resolution enhancement.

Because shift vectors can be calculated section by section, our ISM architecture compensates for different optical distortions and misalignment that can occur during 3D deep imaging (Supplementary Fig. 14). Another case in which the access to raw scanned images is important is that of multi-color ISM (Fig. 3c). Because of the different Stokes shifts of the fluorophores and different system conditions for the two excitation beams used, the shift vectors for different colors are not equal. Because reconstruction is performed a posteriori, pulse-by-pulse, pixel-by-pixel or line-by-line multicolor strategies are straightforward to implement in the proposed ISM architecture.

We have demonstrated a straightforward implementation of ISM based on a novel SPAD array module. This implementation supports any objective lens and maintains optical-sectioning, multicolor, live-cell and deep imaging associated with confocal imaging. Thanks to the access to the raw scanned images, our method extracts parameters that are fundamental to the reconstruction of super-resolution images without calibration or prior information and in the presence of optical distortions or misalignment. More generally, the analysis

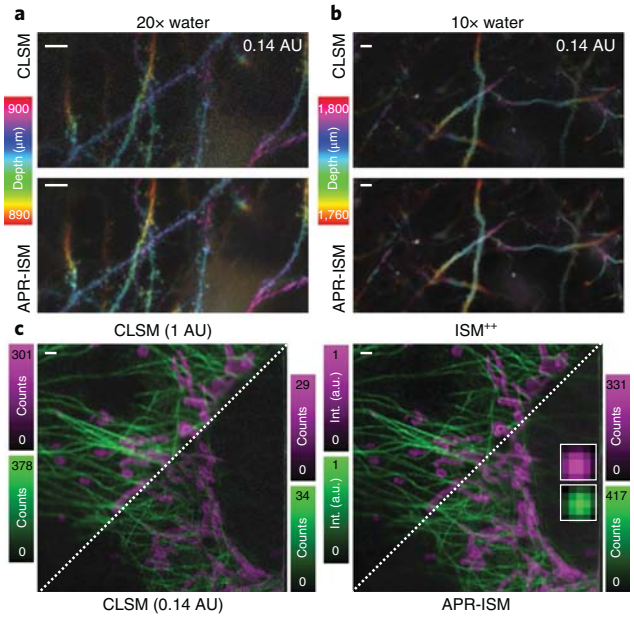

Fig. 3 | Image scanning microscopy with the SPAD array on a commercial confocal system. a,**b**, Deep ISM imaging of neuronal processes in a whole cleared brain of a Thy1-eYFP-H transgenic mouse with 20× (**a**) and 10× (**b**) water-immersion objective lenses. Each panel shows a side-by-side comparison of 'ideal' confocal (top) and APR-ISM (bottom) images of the maximum intensity projection, color-coded by imaging depth. Scale bars, 5 µm. Data are representative of $n=2$ experiments. **c**, Multicolor ISM of Alexa Fluor 488 for microtubules (green) and Alexa Fluor 568 for mitochondria (magenta). Side-by-side comparison of open confocal, ideal confocal, deconvolved ISM^{++} and APR-ISM. Insets show the fingerprint matrices for the two colors. Scale bars, 1 µm. Data are representative of $n=1$ experiment.

of the raw data provides important information regarding the microscope. For example, the fingerprint map (Fig. 1c,d, Supplementary Note 4) encodes information about (i) the PSF, which may lead to novel strategies for adaptive optics[21] and/or novel blind deconvolution algorithms, and (ii) the system misalignment, which can be used for autoalignment procedures. The single-photon timing ability of the SPAD array allows for the integration of ISM with different time-resolved assays, and we have demonstrated its combination with FLIM. However, the architecture can also be used for fluorescence correlation spectroscopy, other fluctuation correlation methods[22] and anti-bunching analysis[23]. Another important temporal characteristic of our SPAD array module is the absence of a frame rate—specifically, each element of the detector array works in parallel. These characteristics make the SPAD array compatible with smart illumination schemes[24] and with fast beam scanners such as the resonant scanner (Supplementary Fig. 15). Resonant scanners are normally combined with photomultiplier tubes because of their higher dynamic range compared with that of SPADs. However, because the photons emitted from each sample position are spread across all the elements of the SPAD array, the effective dynamic range of the SPAD array is considerably higher than those of single elements.

We believe that SPAD arrays can become the standard detectors for versatile and multiparameter ISM, capable of converting any conventional point-scanning microscope into a super-resolution microscope.

Online content

Any methods, additional references, Nature Research reporting summaries, source data, statements of data availability and associated accession codes are available at https://doi.org/10.1038/s41592-018-0291-9.

References

1. Pawley, J.B. (ed.) *Handbook of Biological Confocal Microscopy* (Springer, 1995).
2. Ebrecht, R., Don Paul, C. & Wouters, F. S. *Protoplasma* **251**, 293–305 (2014).
3. Sheppard, C. J. R. *Optik (Stuttg.)* **80**, 53–54 (1988).
4. Sheppard, C. J. R., Mehta, S. B. & Heintzmann, R. *Opt. Lett.* **38**, 2889–2892 (2013).
5. Müller, C. B. & Enderlein, J. *Phys. Rev. Lett.* **104**, 198101 (2010).
6. Castello, M., Sheppard, C. J. R., Diaspro, A. & Vicidomini, G. *Opt. Lett.* **40**, 5355–5358 (2015).
7. York, A. G. et al. *Nat. Methods* **9**, 749–754 (2012).
8. Schulz, O. et al. *Proc. Natl Acad. Sci. USA* **110**, 21000–21005 (2013).
9. De Luca, G. M. et al. *Biomed. Opt. Express* **4**, 2644–2656 (2013).
10. York, A. G. et al. *Nat. Methods* **10**, 1122–1126 (2013).
11. Roth, S., Sheppard, C. J. R., Wicker, K. & Heintzmann, R. *Opt. Nanoscopy* **2**, 5 (2013).
12. Winter, P. W. et al. *Optica* **1**, 181–191 (2014).
13. Gregor, I. et al. *Nat. Methods* **14**, 1087–1089 (2017).
14. Sheppard, C. J. R., Castello, M., Tortarolo, G., Vicidomini, G. & Diaspro, A. *J. Opt. Soc. Am. A Opt. Image Sci. Vis.* **34**, 1339–1350 (2017).
15. Huff, J. *Nat. Methods* **12**, i–ii (2015).
16. Zappa, F., Tisa, S., Tosi, A. & Cova, S. *Sens. Actuators A Phys.* **140**, 103–112 (2007).
17. Becker, W. (ed.) *Advanced Time-Correlated Single Photon Counting Applications* (Springer, 2015).
18. Bertero, M., Boccacci, P., Desider'a, G. & Vicidomini, G. *Inverse Probl.* **25**, 123006 (2009).
19. Tortarolo, G., Castello, M., Diaspro, A., Koho, S. & Vicidomini, G. *Optica* **5**, 32–35 (2018).
20. Owen, D. M. et al. *Biophys. J.* **90**, L80–L82 (2006).
21. Booth, M. J. *Light Sci. Appl.* **3**, e165 (2014).
22. Digman, M. A. & Gratton, E. *Annu. Rev. Phys. Chem.* **62**, 645–668 (2011).
23. Israel, Y., Tenne, R., Oron, D. & Silberberg, Y. *Nat. Commun.* **8**, 14786 (2017).
24. Hoebe, R. A. et al. *Nat. Biotechnol.* **25**, 249–253 (2007).

Acknowledgements

This work was partially supported by the Compagnia di San Paolo (ROL 20641 to G.T. and G.V.). We thank R. Nakamura (Nikon Corporation, Japan) for support with confocal A1R measurements, and Nikon Corporation for sharing useful technical information about confocal A1R and for dual-color (mitochondria and tubulin) sample preparation. We thank R. Kawakami, K. Otomo and T. Nemoto (Research Institute for Electronic Science, Hokkaido University) for advice on whole-brain imaging. We thank F. Cella Zanacchi (Istituto Italiano di Tecnologia) for support in cell preparation, and S. Piazza (Istituto Italiano di Tecnologia), E. Slenders (Hasselt University) and E. Tcarenkova (Turku University) for useful discussions.

Author contributions

M.C. and G.V. conceived the idea. A.T. and G.V. supervised the project, with support from C.J.R.S., P.B. and A.D. M.C., M.B., F.V., A.T. and G.V. designed the SPAD array. M.B., F.V. and A.T. realized and characterized the SPAD array. M.C., G.T. and G.V. designed and implemented the custom ISM system. T.D., P.B. and G.V. integrated the ISM method on the commercial microscope. M.C., G.T. and G.V. designed and developed the controlling architecture. M.C., G.T., S.K. and G.V. developed the image processing and analysis software. M.C., G.T., T.D., M.O., S.P., P.B. and G.V. performed the experiments and analyzed the data with support from all other authors. L.P., M.O., S.P. and L.L. assisted in live-cell imaging and fluorescence lifetime experiments. M.C., G.T. and G.V. wrote the manuscript with input from all other authors.

Competing interests

M.C., G.T., M.B., F.V., P.B., C.J.R.S., A.D., A.T. and G.V. have filed a patent application (application number IT 102018000001891) on the method presented.

Additional information

Supplementary information is available for this paper at https://doi.org/10.1038/s41592-018-0291-9.

Correspondence and requests for materials should be addressed to G.V.

Methods

Custom microscope. We created the custom-made ISM system (Supplementary Fig. 2) by modifying an existing point-scanning microscope previously described in ref. [19]. Briefly, the excitation beams were provided by two triggerable pulsed (~80-ps pulse width) diode lasers (LDH-D-C-640 and LDH-D-C-485; Picoquant) emitting at 640 nm and 485 nm; we controlled their intensity/power with two acoustic optical modulators (AOMs; MT80-A1-VIS; AA Optoelectronic). After being combined by a long/short-pass dichroic mirror (F43-491; AHF Analysentechnik) and reflected by a multi-band dichroic mirror (ZT 405-488-594-640-775; Chroma), the two excitation beams are deflected by two galvanometric scanning mirrors (6215HM40B; CT Cambridge Technology) and directed toward the objective lens (CFI Plan Apo VC 60×/1.4-NA, oil; Nikon) by the same set of scan and tube lenses used in a commercial scanning microscope (Confocal C2; Nikon). The fluorescence light is collected by the same objective lens, descanned, and passed through the multi-band dichroic mirror and then through a suitable fluorescence band-pass filter, depending on the imaging experiment (685/70 nm or 525/50 nm; AHF Analysentechnik). A 300-mm aspheric lens (Thorlabs) focuses the fluorescent light into the pinhole plane, generating a conjugated image plane with a magnification of 300×. For ISM measurements, the pinhole is kept completely open. A telescope system, built using two aspheric lenses of 100-mm and 150-mm focal length (Thorlabs), conjugates the SPAD array with the pinhole and provides an extra magnification factor. The final magnification on the SPAD array plane is 450×, and thus the size of the SPAD array projected on the specimen is ~1.4 AU (at the far-red emission wavelength, i.e., 650 nm) and ~1.7 AU (at the green emission wavelength, i.e., 525 nm). Every photon detected by any of the 25 elements of the SPAD array generates a transistor-transistor logic (TTL) signal that is delivered through the dedicated channel (one channel for each sensitive element of the detector) to a field-programmable-gate-array-based data-acquisition card (NI USB-7856R; National Instruments), which is controlled by our own data-acquisition/visualization/processing software carma. The software package carma also controls all microscope devices needed during the image acquisition, such as the galvanometric mirrors, the axial piezo stage, and the AOMs, and it visualizes the data. In particular, carma synchronizes the galvanometric mirrors with the photon detection to distribute photons between the different pixels of the images. All power values reported for this setup refer to the power measured at the sample plane.

To perform lifetime measurements, we also connected the five central elements of the SPAD array module to a multi-channel time-to-digital converter (TDC) with a temporal jittering of 80 ps (FWHM) and a maximum sustained data rate of 8.5 million tags per second (Time Tagger 20; Swabian Instruments), working in the so-called time-tag modality. We appropriately delayed the electronic trigger output signal provided by the driver of the excitation laser (485 nm or 640 nm, depending on the imaging experiment) running at 80 MHz with a picosecond electronic delayer (Picosecond Delayer; Micro Photon Devices) and used the output as the reference signal (sync) for the time-resolved measurement. The carma microscope control generated the pixel, line and frame clocks, which we sent to the multi-channel TDC. We used a custom software module to read the stream of events outputted by the Time Tagger 20 card, each of them labeled with the corresponding inputs (sync, pixel, line, frame or element 1–5) and the time of arrival (time tag). To reduce the data rate, the card discards all synchronization events (80 MHz) except those that follow after one of the low-rate events, thereby forming a reduced time-tag stream. Once the time-tag stream has been created, for each photon event its micro-time (delay from the sync signal) is calculated and the scanned lifetime histogram images (128 bins, 100 ps each), one for each SPAD element, are generated. The result is a series of three-dimensional scanned images in which the third dimension represents the lag time (photon-arrival time) of the histogram. Relative delays between the different elements of the detector are corrected through measurement of their impulse-response functions.

Commercial microscope. We integrated our SPAD array into a commercial Nikon A1R confocal microscope (Supplementary Fig. 13). We did not modify the optical configuration of the system, but for our ISM detection we took advantage of the extra confocal output port of its scanning head, which is designed for spectral detection. We removed the fiber coupling lens from the output port and placed a motorized zoom lens (Optem FUSION composed of a mini camera tube 3×(f600mm), 7:1 zoom motorized stepper, and lower lens 1×(f200mm); Qioptiq) after the port to conjugate the pinhole plane (inside the scanning head) with the SPAD array. Thanks to the zoom lens, we were able to add extra magnification to the system (1.3–8.7×) to obtain a 1-AU projected size (at the emission wavelength) of the SPAD array for the different objective lenses used in this work: a CFI Apo TIRF 60×/1.49-NA (numerical aperture) oil lens (Nikon), CFI Apo LWD Lambda S 20×/0.95-NA WI (Nikon), and a CFI Plan Apo 10×/0.5-NA C Glyc (Nikon). We calibrated the total magnification of the system for the different settings of the zoom lens and different objective lenses by using an approach based on the estimation of the relative shift between the scanned images (Supplementary Note 2). The system performs multi-color confocal imaging thanks to a laser unit equipped with a series of continuous-wave lasers (405 nm, 488 nm, 561 nm and 640 nm). Fluorescence is filtered by the internal dichroics and band-pass filters (525/50 nm and 595/50 nm) before reaching the SPAD array. Controlling, visualization and processing are performed by the same software/hardware used for the custom system, namely, the carma control unit. Within the Nikon application, carma switches between two modalities, master and slave. In the first modality, carma (i) provides analog signals to the Nikon control unit to conduct the galvanometer mirrors, the stage and the AOMs; (ii) records signal from the SPAD array; and (iii) visualizes and processes the data. In the slave modality, carma (i) receives the reference signal (pixel, line and frame clocks) from the Nikon control unit, which acts as a master to conduct all the devices; (ii) records signal from the SPAD array; and (iii) visualizes and processes the data. The slave modality has been used to implement fast ISM imaging with the resonant scanner.

Image reconstruction and analysis. To reconstruct the high-resolution ISM image, we implemented the PR method (Supplementary Note 2), which consists mainly of (i) shifting each scanned image (i,j) of a shift vector $\mathbf{s}_{i,j}$ and (ii) adding up all the shifted images. The shift vectors can be estimated theoretically on the basis of the geometrical properties of the SPAD array and optical characteristics of the scanning microscope: theoretical shift vectors represent the distance between the SPAD array elements and the 'central' element, scaled by the magnification on the detector, the pixel size of the image and the PR factor, which is equal to 2 in the case of reflection (illumination and detection PSFs are identical). However, in this work, we used a phase-correlation approach[6,25] (Supplementary Note 2) able to automatically estimate the shift vectors directly from the scanned images and to compensate for distortions (misalignments and aberrations) of the system that may arise during imaging (APR-ISM). Notably, the ability to estimate the shift vectors directly from the scanned images is fundamental when one is combining ISM with stimulated emission depletion microscopy[26]: in this case, the excitation and emission PSFs are substantially different, and the former is influenced by many imaging parameters that are difficult to know[19].

Alternatively, the high-resolution ISM image can be reconstructed via a multi-image deconvolution iterative algorithm[27–31] (Supplementary Note 3),

$$\mathbf{f}^{k+1} = \mathbf{f}^{k} \sum_{(i,j)} \left(w_{i,j}^{-1} \mathbf{h}_{i,j} \star \frac{\mathbf{g}_{i,j}}{\mathbf{h}_{i,j} * \mathbf{f}^{k}} \right)$$

where $\mathbf{h}_{i,j}$ is the PSF linked to element (i,j) of the SPAD array, $\mathbf{g}_{i,j}$ is the series of scanned images, $\mathbf{f}^k$ is the reconstructed image at iteration k, and $w_{i,j} = (0, \ldots, 1]$, a scaling factor that takes into account the different SNRs of the images. As PSFs, we used a simple Gaussian model that considers the shift vector calculated via the phase-correlation method. We applied only a few iterations of the algorithm so as to avoid artifacts.

In contrast to the all-optical implementation, our fully automatic reconstruction approaches do not allow true real-time imaging. However, the low computational complexity of the APR-ISM method yields the high-resolution image immediately after scanning. Otherwise, with the use of preloaded shift vectors (e.g., obtained from previously scanned images), the high-resolution image can be reconstructed in real time (pixel by pixel).

In the context of FLISM (Fig. 2), the time-tag data produced by the multi-TDC cards are analyzed to produce a series of 3D scanned images (x,y,t) in which the third dimension t (temporal bin or lag time) represents the photon-arrival-time histogram (Supplementary Fig. 10). The PR method is applied to this series of 3D scanned images for each temporal bin (bin by bin), resulting in a 3D-FLISM dataset. The same shift vectors are used for all temporal bins and are estimated on the 2D scanned images obtained by integration of the photons across the lag time. We finally analyzed the 3D-FLISM/FLIM dataset in the time domain with the FLIMfit software tool developed at Imperial College London (https://www.flimfit.org). In short, the software fits the fluorescence decay trace (i.e., the photon-arrival-time histogram) of each pixel with a single exponential function to extract the fluorescence lifetime τ. Alternatively, we analyzed the 3D FLISM/FLIM data in the frequency domain by using a custom software able to transform the decay trace of each pixel into a pair of values, the phasor point (g,s), for display on the polar/phasor plot[32]. The phasor values are the normalized cosine (g) and sine (s) transforms at modulation frequencies equal to the repetition rate of the excitation laser.

We carried out FRC analysis using a pair of APR-ISM datasets (series of scanned images) registered 'simultaneously' thanks to a pixel dwell-time splitting[1]. The fixed 1/7 threshold was used for the entire analysis.

The PR method, the phasor plot calculation, the multi-image deconvolution method and the FRC analysis were implemented on the carma platform (based on C#) and in Matlab.

Sample preparation. We measured the PSF of our ISM system by using gold beads, and we demonstrated the enhancement in spatial resolution via 2D imaging of fluorescent beads, tubulin filaments, mitochondria, nuclear lamin and nuclear pore complexes. We also performed 3D imaging of an optically cleared mouse brain.

Gold beads. We dropped a solution of 80-nm-diameter gold beads in water onto a poly-L-lysine (Sigma)-coated glass coverslip. Then we mounted it with the same oil used as a medium for the objective lens (Nikon immersion oil).

Fluorescent beads. In this study we used a commercial sample of ATTO 647 N fluorescent beads with a diameter of 23 nm (Gatta-BeadsR; GattaQuant).

Tubulin filament imaging in fixed cells. Human HeLa cells were fixed with ice-cold methanol for 20 min at –20 °C and then washed three times for 15 min in PBS. After 1 h at room temperature, the cells were treated in a solution of 3% bovine serum albumin (BSA) and 0.1% Triton in PBS (blocking buffer). The cells were then incubated with monoclonal mouse anti-α-tubulin antiserum (Sigma-Aldrich) diluted in blocking buffer (1:800) for 1 h at room temperature. The α-tubulin antibody was revealed by Abberior STAR Red goat anti-mouse (Abberior) for the custom microscope or Alexa Fluor 546–conjugated goat anti-mouse (Sigma Aldrich) for the Nikon-based microscope. The cells were rinsed three times in PBS for 5 min.

Dual-color tubulin filaments and mitochondria in fixed cells. After fixation and permeabilization, as described above, BSC-1 cells from African green monkey kidney were incubated with rat anti-tubulin monoclonal antibody (YL1/2; Abcam) and rabbit anti-Tom20 polyclonal antibody (FL-145; Santa Cruz) diluted in blocking buffer at 1:100 and 1:50, respectively, for 1 h at room temperature. Cells were washed with PBS three times for 5 min each time. Secondary antibodies were applied (goat anti-rat IgG (H + L) cross-adsorbed secondary antibody, Alexa Fluor 488 (Thermo Fisher Scientific); goat anti-rabbit IgG (H + L) cross-adsorbed secondary antibody, Alexa Fluor 568 (Thermo Fisher Scientific)) at a dilution of 1:500 for 1 h at room temperature. The cells were then rinsed with PBS five times for 5 min each time.

Nuclear-pore-complex imaging in fixed cells. Human osteosarcoma cells were pre-extracted with 2.4% PFA and 0.3% Triton X-100 in PBS for 3 min. After fixation with 2.4% PFA for 30 min, the cells were blocked for 1 h with 5% BSA. Next, the cells were incubated overnight at 4 °C with mouse anti-Nup107 monoclonal antibody (1:250; Thermo Fisher) in 5% BSA. After several washes in PBS, the cells were incubated with the secondary antibody (Alexa Fluor 488; 1:200) at room temperature for 1 h.

Lamin imaging in fixed cells. Human embryonic kidney (HEK) cells were fixed with ice-cold methanol for 10 min at –20 °C. After incubation in BSA, the cells were incubated with rabbit anti-lamin A polyclonal antibody (1:1,000; Abcam) overnight at 4 °C. After several washes in PBS, the cells were incubated with the secondary antibody (Alexa Fluor 488; 1:200) at room temperature for 1 h.

Mitochondria in live cells. To label mitochondria, we incubated HEK cells with MitoTracker Deep Red FM (Thermo Fisher Scientific) diluted in Live Cell Imaging Solution (LICS; Thermo Fisher Scientific) at 1:10,000 for 30 min at 37 °C and imaged them immediately after at the microscope.

SiR-tubulin in live cells. To label tubulin proteins, we incubated human HeLa cells with a SiR-tubulin kit (Spirochrome) diluted in LICS at a concentration of 1 µM for 30 min at 37 °C and then immediately imaged them with the microscope.

Polarity-sensitive membrane probe in live cells. For live-cell imaging, human prostate carcinoma (PC-3) cells were seeded on multiwell chambered coverslips (Ibidi) at 60–80% confluence. After being washed in PBS, cells were stained with 5 µM Di-4-ANEPPDHQ (Thermo Fisher Scientific) and incubated for 30 min at 37 °C with 5% CO_2.

Optically cleared brain of Thy1-eYFP-H transgenic mouse. The CLARITY method was used to clear the mouse brain[33]. In short, after perfusion, mouse brains were post-fixed in 4% PFA overnight at 4 °C and then immersed in 2% hydrogel (2% acrylamide, 0.125% Bis, 4% PFA, 0.025% VA-044 initiator (w/v), in PBS) for 3 d at 4 °C. Samples were degassed and polymerized for 3.5 h at 37 °C. The samples were removed from hydrogel and washed with 8% SDS for 1 d at 37 °C. The samples were transferred to fresh 8% SDS for 21 d at 37 °C for delipidation. Then the samples were washed with 0.2% PBST for 3 d at 37 °C. Brains were incubated in RapiClear CS (RCCS002; SunJin Lab) for 2–3 d at room temperature for the optical clearing. The objective lens was immersed in water for 20 × imaging and in the clearing solution for 10 × imaging.

Reporting Summary. Further information on research design is available in the Nature Research Reporting Summary linked to this article.

Code availability

The Matlab software for PR, multi-image deconvolution, phasor plot calculation and FRC analysis is freely available for academic use and is provided online with this paper as Supplementary Software.

Data availability

The data that support the findings of this study are available from the corresponding author. Source data for Fig. 1 and Supplementary Figs. 3–6 are available online.

References

25. Yu, Z., Liu, S., Zhu, D., Kuang, C. & Liu, X. *Opt. Commun.* **404**, 139–146 (2017).
26. Vicidomini, G., Bianchini, P. & Diaspro, A. *Nat. Methods* **15**, 173–182 (2018).
27. Vicidomini, G., Schmidt, R., Egner, A., Hell, S. & Schönle, A. *Opt. Express* **18**, 10154–10167 (2010).
28. Ingaramo, M. et al. *ChemPhysChem* **15**, 794–800 (2014).
29. Castello, M., Diaspro, A. & Vicidomini, G. *Appl. Phys. Lett.* **105**, 234106 (2014).
30. Koho, S., Deguchi, T. & Hänninen, P. E. *J. Microsc.* **260**, 208–218 (2015).
31. Ströhl, F. & Kaminski, C. F. *Methods Appl. Fluoresc.* **3**, 014002 (2015).
32. Digman, M. A., Caiolfa, V. R., Zamai, M. & Gratton, E. *Biophys. J.* **94**, L14–L16 (2008).
33. Chung, K. et al. *Nature* **497**, 332–337 (2013).